

Imaging electrostatically confined Dirac fermions in graphene quantum dots

3 Juwon Lee, Dillon Wong, Jairo Velasco Jr., Joaquin F. Rodriguez-Nieva, Salman Kahn, Hsin-
4 Zon Tsai, Takashi Taniguchi, Kenji Watanabe, Alex Zettl, Feng Wang, Leonid S. Levitov and
5 Michael F. Crommie

6

7 TABLE OF CONTENTS:

8 **S1. Estimating the curvature of the quadratic potential**

9 **S2. $dI/dV_s(V_g, V_s)$ and $dI/dV_s(r, V_s)$**

10 **S3. $d^2I/dV_s^2(V_g, V_s)$ and $d^2I/dV_s^2(r, V_s)$ for opposite polarity pn junctions**

11 **S4. Procedure for creating a graphene quantum dot**

12 **S5. Tip height dependence in dI/dV_s maps**

13 **S6. Resonance widths**

14

15 **S1. Estimating the curvature of the quadratic potential**

16 We modelled our pn junction using the 2D massless Dirac Hamiltonian with a quadratic
17 potential, $H = -i\hbar v_F \boldsymbol{\sigma} \cdot \nabla_r - \kappa r^2$. We chose $\kappa = 6 \times 10^{-3}$ meV/nm², and the resulting
18 theoretical simulation (Fig. 4b of the main text) is in good agreement with the experimental data
19 (Fig. 4a of the main text). This value for κ was not chosen arbitrarily. We estimated κ through
20 scanning tunnelling spectroscopy (STS) measurements of the Dirac point, with the assumption
21 that the potential varies slowly enough that the Thomas-Fermi approximation is valid. At each
22 point r away from the centre we performed a dI/dV_s measurement at fixed V_g such that E_D is
23 outside of the inelastic tunnelling gap (to do this we needed to use a value of V_g that is different

24 from the value $V_g = 32$ V used for the data presented in Fig. 4a of the main text). We then
 25 extracted E_D through a parabolic fit, converted E_D to charge carrier density through $n(r) =$
 26 $E_D^2(r)/\pi(\hbar v_F)^2$, and rigidly shifted the entire $n(r)$ curve by a uniform constant to match the data at
 27 $V_g = 32$ V (i.e. the gate voltage in Fig. 4a of the main text). The resulting shifted $n(r)$ is plotted in
 28 Fig. S1a, and the equivalent E_D is plotted as the blue curve in Fig. S1b. A similar procedure was
 29 used to construct the $n(x,y)$ plot in Fig. 1c of the main text (with the E_D measurement performed
 30 at $V_g = 50$ V, and then $n(x,y)$ shifted to match the gate voltage held during the tip pulse).
 31 Although the data in Figs 2 and 4a of the main text are obtained from the same pn junction, the
 32 data in Fig 1c is from a different but identically prepared pn junction.

33 The blue curve in Fig. S1b is an approximate representation of the potential felt by Dirac
 34 quasiparticles in the pn junction of Figs 2 and 4a of the main text. We extract κ by fitting the
 35 blue curve in Fig. S1b with an even quadratic polynomial (red curve). This procedure results in
 36 $E_D(r) = (-6.33 \times 10^{-6} \text{ eV/nm}) r^2 + (1.05 \times 10^{-1} \text{ eV})$, yielding $\kappa = 6 \pm 1 \times$
 37 10^{-3} meV/nm^2 (corresponding to characteristic energy $\varepsilon^* = (\hbar^2 v_F^2 \kappa)^{1/3} \approx 15 \text{ meV}$ and
 38 characteristic length $r^* = (\hbar v_F / \kappa)^{1/3} \approx 50 \text{ nm}$).

39 Although the potential in Fig. S1b (blue curve) deviates from the parabolic fit (red curve),
 40 this does not appear to significantly affect the agreement between the experimental and
 41 theoretical eigenstate distributions in Figs 4a and 4b of the main text. In order to understand how
 42 deviations from a parabolic potential affect our results, we simulated $\partial \text{LDOS} / \partial \varepsilon$ for a non-
 43 parabolic potential $U(r)$ whose carrier density is given by a generic shifted power law function:

$$n(r) = n_\infty - \frac{n_0}{(1 + (r/d)^2)^\gamma}$$

44 Here $n_\infty = 6 \times 10^{12} \text{ cm}^{-2}$, $n_0 = 6.9 \times 10^{12} \text{ cm}^{-2}$, and $d = 400 \text{ nm}$ are phenomenological
 45 parameters determined by fitting to the experimental potential. For simplicity, we chose $\gamma = \frac{3}{2}$

46 (which happens to be the power law for the perfect screening of charge spatially separated from
 47 graphene¹). In the Thomas-Fermi approximation, the potential is given by

$$U(r) = \text{sgn}(n(r))\hbar v_F \sqrt{\pi|n(r)|}$$

48 The above equations for $U(r)$ and $n(r)$ fit the experimental potential quite nicely over the entire
 49 spatial range of the measurement (see green curve in Fig. S1b for fit). The resulting $\partial\text{LDOS}/\partial\varepsilon$
 50 calculated for this potential (inset in Fig. S1b) is qualitatively and quantitatively similar to
 51 $\partial\text{LDOS}/\partial\varepsilon$ calculated for the parabolic potential (Fig. 4b of the main text). As such, the simple
 52 parabolic potential model is sufficient to explain our experimental results.

53 **S2. $dI/dV_s(V_g, V_s)$ and $dI/dV_s(r, V_s)$**

54 Figs 2d-g of the main text show $d^2I/dV_s^2(V_g, V_s)$ measurements that were obtained by
 55 numerically differentiating $dI/dV_s(V_g, V_s)$. Fig. S2 shows a plot of $dI/dV_s(V_g, V_s)$ before
 56 differentiation. The red streak in the lower right corner of each plot in Fig. S2 persists inside and
 57 outside the pn junction. This spectroscopic feature may be related to graphene plasmons²⁻⁴.

58 Fig. 4a of the main text shows a $d^2I/dV_s^2(r, V_s)$ measurement that was obtained by
 59 numerically differentiating $dI/dV_s(r, V_s)$. Fig. S3a shows a plot of $dI/dV_s(r, V_s)$ before
 60 differentiation, and Fig. S3c shows dI/dV_s line cuts at fixed radial distances.

61 **S3. $d^2I/dV_s^2(V_g, V_s)$ and $d^2I/dV_s^2(r, V_s)$ for opposite polarity pn junctions**

62 Figs 2d-g of the main text shows $d^2I/dV_s^2(V_g, V_s)$ for a pn junction that is p-doped at the
 63 centre and n-doped outside. Figs S4a-d show $dI/dV_s(V_g, V_s)$ for a pn junction of the opposite
 64 heterojunction polarity (i.e. n-doped at the center and p-doped outside), and Figs S4e-h show the
 65 numerically differentiated $d^2I/dV_s^2(V_g, V_s)$.

66 Fig. S5a shows $dI/dV_s(r, V_s)$ for a pn junction that is n-doped at the centre and p-doped
 67 outside, and Fig. S5b shows $d^2I/dV_s^2(r, V_s)$. For reasons that we do not fully understand, n-doped

68 quantum dots show poorer confinement features than the p-doped quantum dots. Nevertheless,
69 all of our graphene quantum dots display similar oscillatory behaviour in the local density of
70 states, with reasonably similar characteristic spatial widths and energy spacings between discrete
71 states.

72 The pn junction in Fig. 3 of the main text is also n-doped at the centre and p-doped
73 outside. Figs 3a and 3b of the main text are dI/dV_s maps of the same pn junction for different V_s
74 and V_g , with the eigenstate in Fig. 3b having energy approximately 15 mV greater than in Fig.
75 3a. The pn junctions in Fig. S4, Fig. S5, and Fig. 3 of the main text are all different but are
76 prepared in a similar manner (tip pulse at $V_g = -40$ V, $V_s = 5$ V).

77 **S4. Procedure for creating a graphene quantum dot**

- 78 1. Set $V_s = -0.5$ V and $I = 0.5$ nA. Close the scanning tunnelling microscope (STM)
79 feedback loop.
- 80 2. To create a graphene quantum dot that is p-doped (n-doped) at the centre, set $V_g = 40$ V (-
81 40 V). Using other values of V_g will lead to different values of doping.
- 82 3. Open the STM feedback loop.
- 83 4. Withdraw the STM tip by $\Delta z \sim 1.5 - 2$ nm.
- 84 5. Increase V_s to +5 V.
- 85 6. Wait 1 minute.
- 86 7. Decrease V_s to -0.5 V.
- 87 8. Close the STM feedback loop.

88 **S5. Tip height dependence in dI/dV_s maps**

89 A dI/dV_s map (at a fixed V_s) measures the local density of states (LDOS) as a function of (x,y) :

$$\frac{dI}{dV_s}(x, y) = A(z) * \text{LDOS}(x, y, z_0, E_F + eV_s)$$

90 where $A(z)$ is a proportionality factor that depends on the tip-sample distance (and z_0 is a fixed
 91 tip-sample distance). Since the dI/dV_s map in Fig. 2c of the main text was obtained using
 92 constant-current feedback, the tip height z will change as a function of (x, y) to ensure

$$I_0 = \left| \int_0^{V_s} \frac{dI}{dV} dV \right| = A(z) \left| \int_0^{V_s} \text{LDOS}(x, y, z_0, E_F + eV) dV \right|$$

93 where $I_0 = 0.5$ nA is the tunnelling current setpoint. Therefore

$$A(z) = \frac{I_0}{\left| \int_0^{V_s} \text{LDOS}(x, y, z_0, E_F + eV) dV \right|}$$

94 and thus

$$\frac{dI}{dV_s}(x, y) = I_0 \frac{\text{LDOS}(x, y, z_0, E_F + eV_s)}{\left| \int_0^{V_s} \text{LDOS}(x, y, z_0, E_F + eV) dV \right|}$$

95 It is clear that dI/dV_s is related to LDOS but is not directly proportional to LDOS (see Wittneven
 96 *et al.*⁵ for more details). This explains the contrast between the p-doped and n-doped regions in
 97 Fig. 2c of the main text. Figure S6 shows two dI/dV_s curves at $r = 0$ nm (blue curve) and $r = 200$
 98 nm (red curve). Both curves have a ~ 130 meV gap-like feature at the Fermi energy caused by
 99 phonon-assisted inelastic tunnelling⁶ and a local minimum (labelled by coloured arrows) that
 100 indicate the Dirac point. Note that dI/dV_s is adjusted such that the area under both curves from V_s
 101 $= -0.25$ V to $V_s = 0$ V is equal to $I_0 = 0.5$ nA (this is the constant-current feedback condition),
 102 resulting in higher dI/dV_s at $V_s = -0.25$ V (the tunnelling bias setpoint for Fig. 2c of the main text)
 103 for the n-doped curve compared to the p-doped curve.

104 S6. Resonance widths

105 A confined state in an electrostatic graphene quantum dot is quasi-bound in the sense that
106 it has a finite lifetime τ due to coupling to the continuum via Klein tunnelling. This “leakage” of
107 the quantum dot can be quantified via the widths of the resonance peaks \hbar/τ . To accurately
108 obtain the intrinsic widths, we chose a simulation size L and Lorentizan broadening $\Gamma \sim \hbar v_F/L$
109 such that $\Gamma < \hbar/\tau$ (see Methods). Except for the $(0, \frac{1}{2})$ state (which has a width ~ 15 meV in
110 theory and experiment), the linewidths in both the experimental data and the simulation lie in the
111 range $4 \text{ meV} \leq \text{width} \leq 10 \text{ meV}$ (corresponding to lifetimes $2 \times 10^{-13} \text{ s} \geq \tau \geq 7 \times 10^{-14} \text{ s}$), with
112 resonances that exhibit higher angular momenta displaying lower widths (longer lifetimes) than
113 states with lower angular momenta. This is consistent with the idea that (due to Klein tunnelling)
114 higher angular momentum states are more easily trapped by circular electrostatic potentials in
115 graphene^{7,8}.

116 Although our experimental and theoretical resonance widths are in good agreement,
117 future studies may be required to fully disentangle the lifetimes due to Klein tunnelling and
118 many-body effects. For example, angle-resolved photoemission spectroscopy (ARPES)⁹ and
119 theoretical calculations¹⁰ have shown that the contribution to the imaginary part of the electron
120 self-energy from electron-electron interactions can be significant in the energy range of our
121 scanning tunnelling spectroscopy experiments.

122

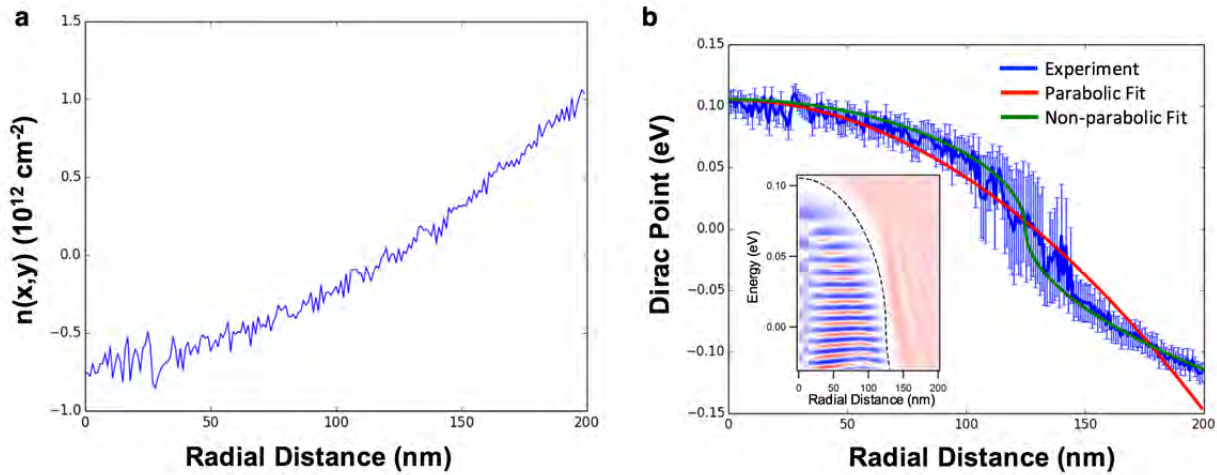
- 123 1. Fogler, M.M., Novikov, D.S. & Shklovskii, B.I. Screening of a hypercritical charge in
124 graphene. *Phys. Rev. B* **76**, 233402 (2007).
- 125 2. Bostwick, A. *et al.* Observation of Plasmarons in Quasi-Freestanding Doped Graphene.
126 *Science* **328**, 999-1002 (2010).
- 127 3. Principi, A., Polini, M., Asgari, R. & MacDonald, A.H. The tunneling density-of-states of
128 interacting massless Dirac fermions. *Solid State Commun.* **152**, 1456-1459 (2012).
- 129 4. Lischner, J., Vigil-Fowler, D. & Louie, S.G. Physical Origin of Satellites in Photoemission of
130 Doped Graphene: An *Ab Initio* GW Plus Cumulant Study. *Phys. Rev. Lett.* **110**, 146801
131 (2013).

- 132 5. Wittneven, C., Dombrowski, R., Morgenstern, M. & Wiesendanger, R. Scattering States
133 of Ionized Dopants Probed by Low Temperature Scanning Tunneling Spectroscopy. *Phys.*
134 *Rev. Lett.* **81**, 5616-5619 (1998).
- 135 6. Zhang, Y. *et al.* Giant phonon-induced conductance in scanning tunnelling spectroscopy
136 of gate-tunable graphene. *Nature Phys.* **4**, 627-630 (2008).
- 137 7. Wu, J.-S. & Fogler, M.M. Scattering of two-dimensional massless Dirac electrons by a
138 circular potential barrier. *Phys. Rev. B* **90**, 235402 (2014).
- 139 8. Zhao, Y. *et al.* Creating and probing electron whispering-gallery modes in graphene.
140 *Science* **348**, 672-675 (2015).
- 141 9. Siegel, D.A. *et al.* Many-body interactions in quasi-freestanding graphene. *Proc. Natl*
142 *Acad. Sci. USA* **108**, 11365-11369 (2011).
- 143 10. Brar, V.W. *et al.* Observation of Carrier-Density-Dependent Many-Body Effects in
144 Graphene via Tunneling Spectroscopy. *Phys. Rev. Lett.* **104**, 036805 (2010).
- 145

146

147 **FIGURE S1**

148



149

150

151 **Figure S1 | Circular electrostatic potential.** **a**, Charge carrier density for the pn junction in Fig.

152 2 and Fig. 4a of the main text. **b**, Dirac point energy (blue curve) corresponding to **a**. The Dirac

153 point energy is fit with a quadratic polynomial with curvature $\kappa = 0.006 \text{ meV/nm}^2$ (red curve).

154 This value of κ is used to generate the theoretical simulation in Fig. 4b of the main text. The

155 green curve is a shifted power law fit to the experimental blue curve. The inset is $\partial\text{LDOS}/\partial\varepsilon$

156 calculated for the non-parabolic potential represented by the green curve (which is also the

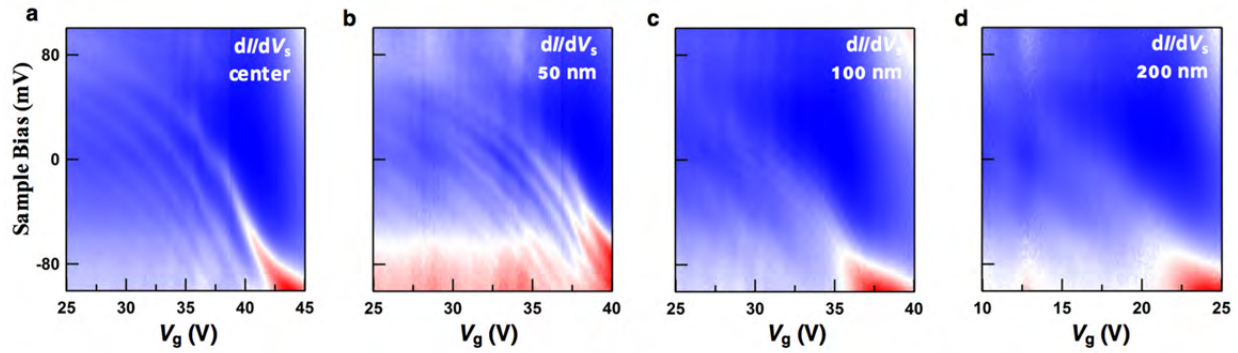
157 dashed line in the inset).

158

159

160 **FIGURE S2**

161



162

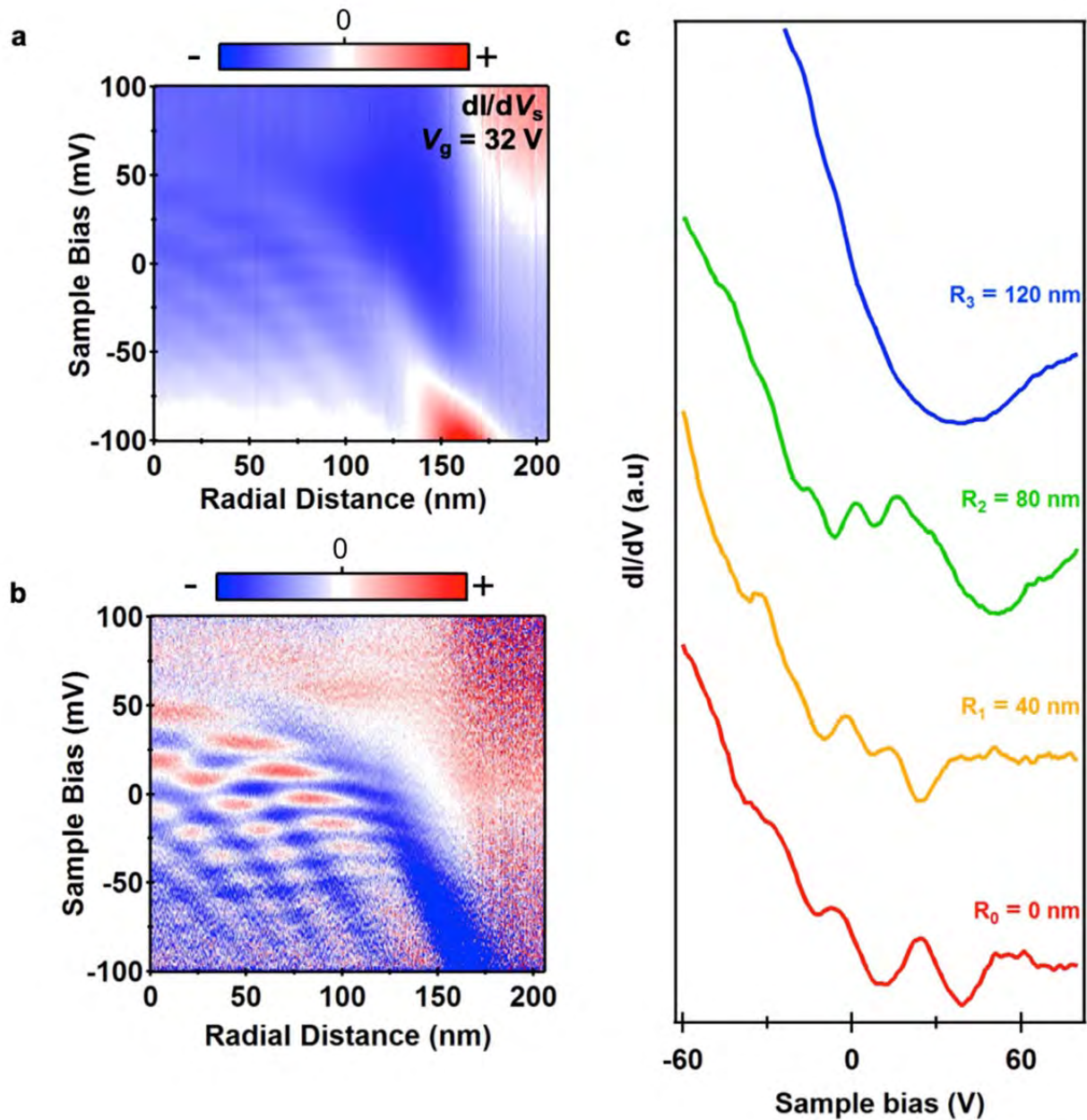
163

164 **Figure S2 | $dI/dV_s(V_g, V_s)$ plots used to calculate $d^2I/dV_s^2(V_g, V_s)$ shown in Figs 2d-g of the**165 **main text.**

166

167

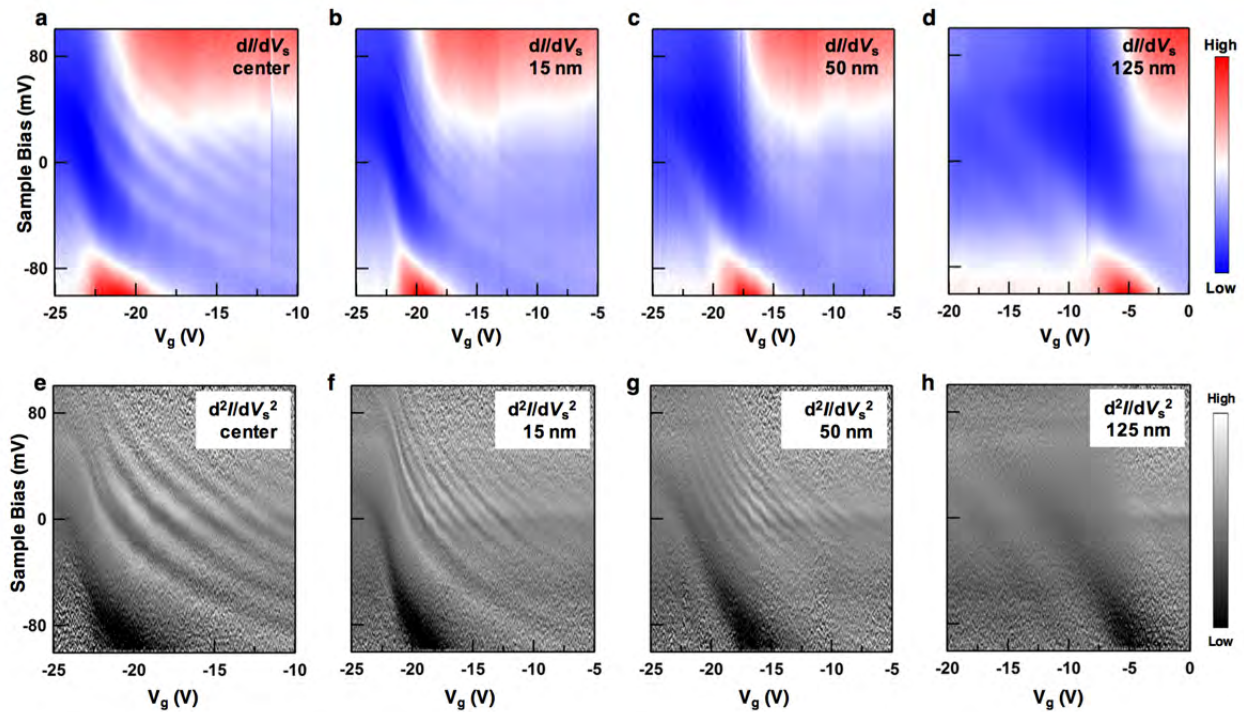
168 **FIGURE S3**



169
 170
 171 **Figure S3 | $dI/dV_s(r, V_s)$ plot used to calculate $d^2I/dV_s^2(r, V_s)$ shown in Fig. 4a of the main**
 172 **text. a, $dI/dV_s(r, V_s)$ plot showing faint horizontal features modulated by a parabolic envelope. b,**
 173 **$d^2I/dV_s^2(r, V_s)$ obtained by numerically differentiating a. c, dI/dV_s line cuts at fixed radial**
 174 **distances showing discrete states at fixed energies.**

175 **FIGURE S4**

176



177

178

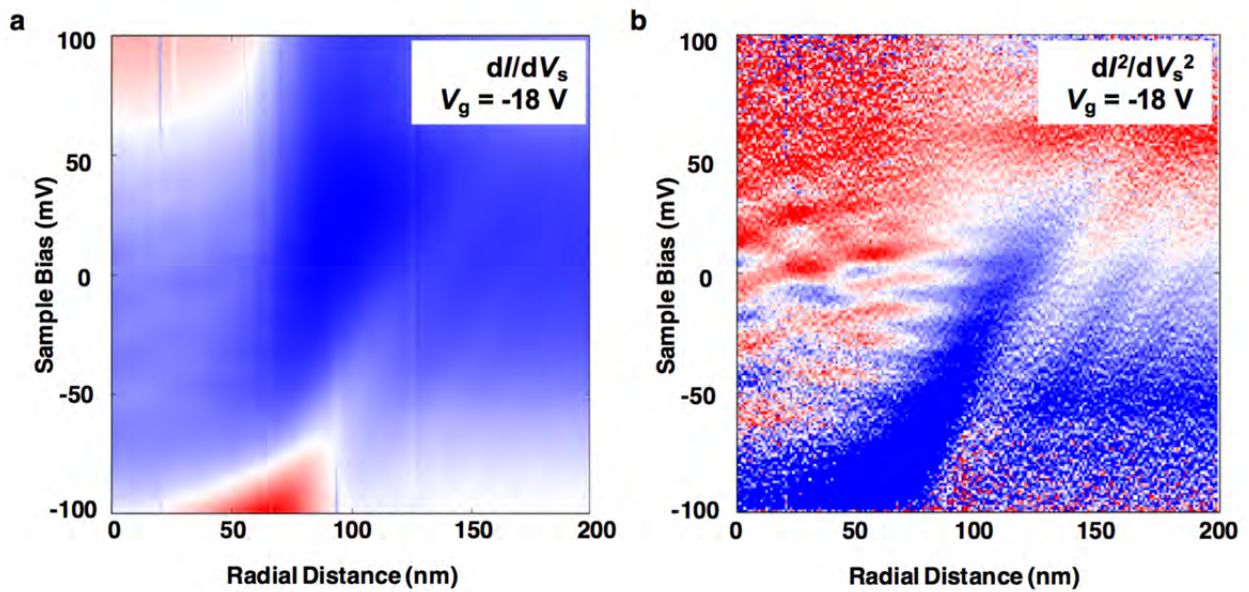
179 **Figure S4 | Gate-tunable STS measurements of pn junction with opposite polarity. a-d,**180 $dI/dV_s(V_g, V_s)$ for a pn junction that is n-doped at the centre and p-doped outside. **e-f,**181 $d^2I/dV_s^2(V_g, V_s)$ obtained by numerically differentiating **a-d**.

182

183

184 **FIGURE S5**

185



186

187

188 **Figure S5 | Spatially resolved energy level spectrum of pn junction with opposite polarity.**

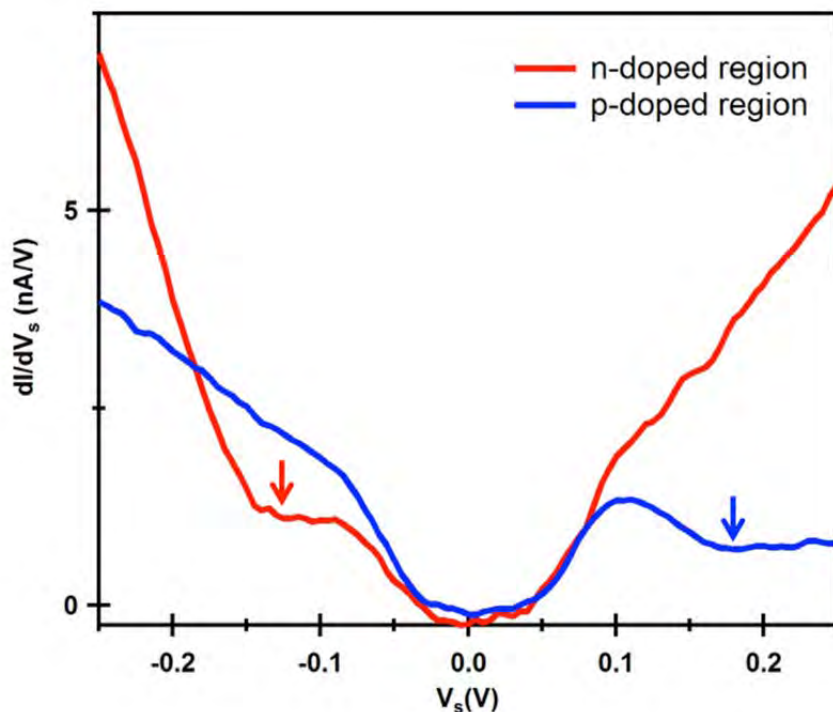
189 **a**, $dI/dV_s(r, V_s)$ for a pn junction that is n-doped at the centre and p-doped outside. **b**,

190 $d^2I/dV_s^2(r, V_s)$ obtained by numerically differentiating **a**.

191

192 **FIGURE S6**

193



194

195

196 **Figure S6 | dI/dV_s curves showing a pn junction.** The blue curve is obtained at the centre ($r =$ 197 0 nm) of the pn junction in Fig. 2c of the main text. The red curve is obtained at $r = 200$ nm

198 away from the centre. The coloured arrows represent the local graphene Dirac point. Note the

199 scaling such that the V_s -integrated area under both curves from $V_s = -0.25$ V to $V_s = 0$ V is equal200 to $I_0 = 0.5$ nA, reflecting the constant-current feedback condition employed in standard STM201 operation. This results in higher dI/dV_s at $V_s = -0.25$ V (the tunnelling bias setpoint for Fig. 2c of202 the main text) for the red curve ($r = 200$ nm) compared the blue curve ($r = 0$ nm).